Magnetic Resonance in Medicine 63:1594–1600 (2010)

Super-Resolved Spatially Encoded Single-Scan 2D MRI

Noam Ben-Eliezer,[1] Michal Irani,[2] and Lucio Frydman[1]*

Single-scan MRI underlies a wide variety of clinical and research activities, including functional and diffusion studies. Most common among these "ultrafast" MRI approaches is echo-planar imaging. Notwithstanding its proven success, echo-planar imaging still faces a number of limitations, particularly as a result of susceptibility heterogeneities and of chemical shift effects that can become acute at high fields. The present study explores a new approach for acquiring multidimensional MR images in a single scan, which possesses a higher built-in immunity to this kind of heterogeneity while retaining echo-planar imaging's temporal and spatial performances. This new protocol combines a novel approach to multidimensional spectroscopy, based on the spatial encoding of the spin interactions, with image reconstruction algorithms based on super-resolution principles. Single-scan two-dimensional MRI examples of the performance improvements provided by the resulting imaging protocol are illustrated using phantom-based and in vivo experiments. Magn Reson Med 63:1594–1600, 2010. © 2010 Wiley-Liss, Inc.

Key words: single-scan imaging; super-resolution; ultrafast MRI; spatial encoded imaging; susceptibility compensation; EPI

The last decades have witnessed a continuous growth in the use of single-scan MRI, both for clinical and research applications (1,2). These "ultrafast" protocols play an essential role in experiments demanding high temporal resolution like functional MRI (3–5); they also constitute integral components in high-dimensionality experiments such as diffusion tensor imaging (6). Foremost among the sequences enabling the acquisition of MR images in a single scan stands echo-planar imaging (EPI) (7), with its many different variants (8,9). EPI relies on a single excitation of all spins within the volume to be examined, followed by repetitive gradient oscillations that scan, in a single continuous $\vec{k}$ acquisition, large regions of the image conjugate ($\vec{k}$-space) domain. The $\rho(\vec{r})$ spin density profile being sought is then retrieved by a numerical Fourier transform (FT) of the digitized information. Notwithstanding their real-time image-gathering capabilities, EPI-based protocols are still challenged by the relatively long data sampling times that they involve. These are ca. an order of magnitude longer than those typically involved in multiscan MRI and expose the protocol to progressive temporal artifacts arising from susceptibility variations, from unfavorable shimming conditions, or from chemical shift heterogeneities. These in turn put practical limitations to the organs and/or conditions that can be studied using ultrafast MRI protocols.

By contrast to EPI's reliance on contributions arising simultaneously from the entire sample, we have recently begun exploring the consequences of relying on a progressive spatial encoding of MR images. Central in the development of these new experiments is the spatiotemporal manipulation of the spin interactions, a concept that originated from a search for methods capable of delivering arbitrary multidimensional MR spectra in a single scan (10,11). The generality of the ensuing approach eventually led to several new routes for executing single-scan multidimensional MRI (12–16). Contrary to EPI, these new MRI methods were found to be local in nature in the sense that, at each instant, the spins' signal $S(t)$ becomes proportional to the density profile $\rho(\vec{r})$ within a limited region of the volume of interest. It follows that spatially encoded methods do not require FT processing for delivering their imaging information: the signal's magnitude, $|S(t)|$, *is* the image being sought. We and others have discussed elsewhere how this property, which in turn is closely linked to experiments put forward by Kunz and Pipe decades ago (17–19), allows spatially encoded MRI to cope efficiently with field inhomogeneities and to deal simultaneously with multiple sites possessing different chemical shifts (14–16). These advantages, however, were also found to materialize at a decreased efficiency in terms of the spatial encoding's use of the acquisition time variable, which usually results in spatial resolution penalties. In this study, we introduce a way of solving these deficiencies. Figure 1 illustrates the ensuing benefits with an in vivo example, showing how *super-resolution algorithms* (SR) and spatially encoded methods can be combined to retrieve high-quality two-dimensional (2D) MR images. The resulting single-scan data possess spatial and temporal resolutions comparable to those achieved by EPI, but a much higher immunity to frequency-dispersing artifacts. The following paragraphs discuss how SR algorithms (20,21)—which find widespread use in microscopy scenarios to "break" wavelength-imposed diffraction limits (22), as well as in compensating motion-related artifacts (23)—couple in a natural way to the time-dependent spin evolution involved in spatially encoded MRI. We then present ways for executing and processing this kind of experiment and demonstrate the multiple advantages of the resulting method when attempting to carry out single-scan MRI under a variety of conditions that challenge conventional EPI's usual capabilities.

[1]Chemical Physics Department, Weizmann Institute, Rehovot, Israel.

[2]Computer Sciences Department, Weizmann Institute, Rehovot, Israel.

*Correspondence to: Lucio Frydman, Ph.D., Chemical Physics Department, Weizmann Institute, 76100 Rehovot, Israel. E-mail: lucio.frydman@weizmann.ac.il

Received 9 September 2009; revised 9 December 2009; accepted 6 January 2010.

DOI 10.1002/mrm.22377

Published online in Wiley InterScience (www.interscience.wiley.com).

© 2010 Wiley-Liss, Inc.

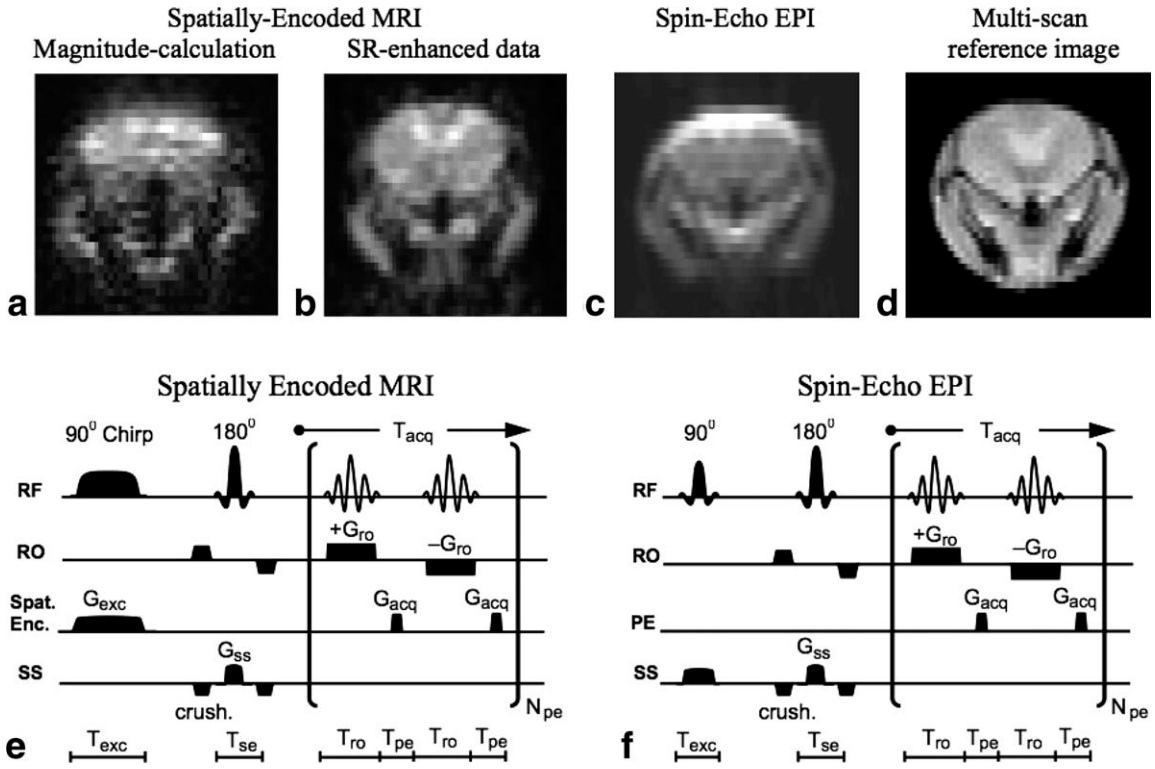

FIG. 1. Top: Single-scan in vivo images of a mouse brain (field of view = 15 × 15mm^2) for (**a**) a magnitude-processed spatially encoded MRI experiment (0.5mm slice; T_{exc} = 3 ms; R = 37 kHz/ms; T_{se} = 4 ms; T_{acq} = 15 ms; Δx = 0.5mm; Δy = 0.5mm). **b**: Idem as in (**a**) but following a SR reconstruction. **c**: An EPI acquisition (1mm slice; T_{exc} = 2 ms; T_{se} = 4 ms; T_{acq} = 18 ms; Δx = 0.5mm; Δy = 0.65mm). **d**: A reference multiscan gradient-echo image (acquisition time = 30 sec). Bottom: Basic 2D single-scan pulse sequences compared in this work; in all instances described in this work, images are displayed with their *y* (vertical) axes corresponding to the spatially encoded dimension, the *x* (horizontal) axis arising from FT of conventional RO data, and their *z* axis associated to the slice-selected (SS) pulse. **e**: Hybrid 2D spatial-/frequency-encoded acquisition. **f**: Blipped spin-echo EPI. In both cases, the overall acquisition time is $T_{acq} = 2(T_{ro}+T_{pe})N_{pe}$ (further experimental and numerical details are provided in the text). Abbreviations: exc: spatially encoded excitation, se: spin-echo, ro: readout direction, pe: phase-/spatially encoded direction, acq: acquisition, N_{pe}: number of phase-encode lines.

THEORY

The Connection Between Spatially Encoded MRI and SR

As mentioned, conventional MRI retrieves the spin density profile $\rho(\vec{r})$ by FT of a *k*-space signal $S(\vec{k}(t))$. Using as working example a one-dimensional *y*-axis imaging case, one would then have $\rho(y) = \int S(k)e^{-iky}dk$, where $k(t) = \gamma \int G_{acq}(\tau)d\tau = \gamma G_{acq}t$ is a wave number defined by the acquisition y-gradient action. By contrast, the imaging scheme we focus upon here relies on a spatially dependent excitation and on directly detecting the spin density profile at sequential locations along the y-axis. The spatially progressive spin excitation required by this scheme can be achieved by sweeping a radiofrequency pulse while in the presence of a field gradient G_{exc} that spreads the spins offsets throughout the field of view L_y (17–19). The effective spin-nutation angles associated with this type of excitation are determined according to the radiofrequency's power. For an excitation time T_{exc} and sweeping over a frequency range of $\gamma G_{exc}L_y$, this power becomes solely a function of the sweep rate $R = \gamma G_{exc}L_y/T_{exc}$ (12). When properly tuned, such swept radiofrequency excitation imposes on the spins a quadratic phase profile given for a refocused 90° nutation by (13):

$$\phi_{exc}(y) = -\frac{\gamma^2 G_{exc}^2}{2R}y^2 + \frac{\gamma^2 G_{exc}^2 L_y}{2R}y - \frac{\gamma^2 G_{exc}^2 L_y^2}{4R}. \quad [1]$$

This phase allows one to reconstruct $\rho(y)$ directly by taking magnitude of a signal $S(t)$, acquired in the presence of the gradient G_{acq}. Indeed, assuming for simplicity that G_{acq} is constantly applied over an acquisition time T_{acq} fulfilling $|G_{exc}T_{exc}| = |G_{acq}T_{acq}|$ (thereby allowing the acquired signal to fully unravel the encoded field of view L_y (12)), the acquisition process adds onto Eq. 1 an additional term $\phi_{acq}(y,t) = \gamma G_{acq}\, t \cdot y = k(t) \cdot y$, leading to an overall time-dependent signal

$$S(t) \propto \int_{L_y} \rho(y) \cdot e^{i\phi_{exc}(y)} e^{i \cdot k(t) y} dy. \quad [2]$$

Given the quadratic *y*-dependence of ϕ_{exc}, the spins phase will vary rapidly across the sample, except at a single stationary phase point where the first spatial derivative of the overall phase vanishes: $\frac{d\phi_{exc}(y)}{dy} + k(t) = 0$. According to this stationary-phase approximation (24), only spins within close vicinity of this time-dependent *y* point will have their magnetizations in phase and

contribute to the observable $S(t)$. The signal modulus thus reflects the spin density profile at a single voxel, according to (12,13):

$$|S(t)| \propto \Delta y \cdot \rho(y). \quad [3]$$

Here Δy denotes the pixel size associated with this method and relates to the second spatial derivative of the phase arising from the initial excitation according to

$$\Delta y = \sqrt{\frac{2\pi}{\left(\frac{d^2\phi_{exc}}{dy^2}\right)}} = \frac{\sqrt{R}}{\gamma G_{exc}} \quad \forall y. \quad [4]$$

Equation 4 implies that the curvature (i.e., the "sharpness") of the parabolic phase profile $\phi_{exc}(y)$ will define the final pixel size Δy of the image (12,13). This is in contrast to FT-based MRI methods, where the pixel size is given by acquisition criteria, rather than at the excitation stage, as in this case.

Figure 2a and b summarizes graphically the temporal evolution of the parabolic phase profile imparted on the spins during the course of the experiment. As only spins located in the slowest-changing regions of these spatially dependent phase profiles will contribute to the observed signal, it follows that the overall phase $\phi_{exc}(y) + \phi_{acq}(y,t)$ defines a "focus" that progressively displaces throughout the acquisition, from one end of the sample to the other. Only within this relatively flat region of the phase profile will the spins interfere constructively toward the macroscopic observable signal, unraveling in the process the local image intensity.

The fact that the spatial resolution in this image-generating protocol is imposed during the relatively short excitation process implies that, unless undesirably large excitation gradients or long encoding times are used, its definition will generally be inferior to that of FT-based methods. The time-dependencies in Fig. 2a and b, however, also hint as to how SR-based methods could assist in solving this limitation. SR algorithms improve the quality of images based on oversampling considerations. These can arise from the availability of multiple images originating from different sources, or from the processing of a single time-dependent image whose acquisition has been overdigitized. In the case illustrated in Fig. 2, the small displacements of the parabolic phase profiles taking place between each acquisition event (corresponding to the increments imposed by G_{acq} in the 2D sequence illustrated in Fig. 1e) implies that these will overlap with one another. This scheme constitutes a kind of oversampling, not of the typical sort, happening because of rapid digitization of an emitted signal using a fast receiver, but rather associated to a redundancy in information arising as the spins' parabolic phase profile progresses and gradually unravels the spatially encoded information. This in turn provides a natural framework for exploiting the power of time-dependent SR, particularly of those algorithms designed to deconvolve information out of a moving "focus", without suffering from the constraints that are usual in fast FT and/or from the limitations imposed by a simple magnitude-calculation based on the stationary-phase approximation.

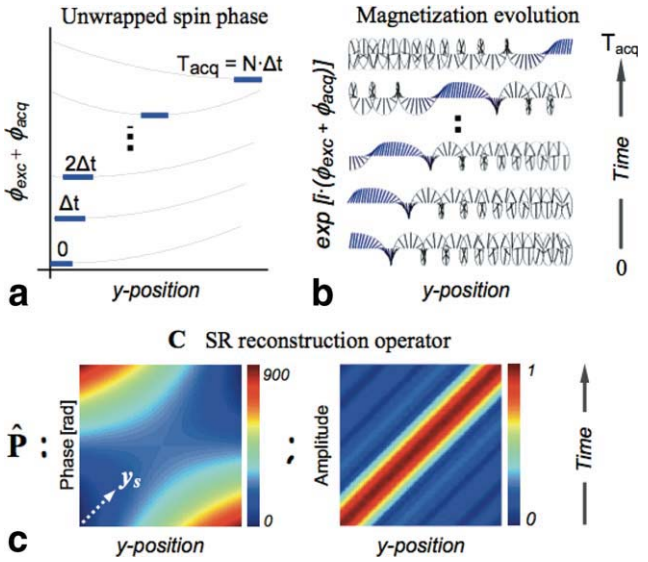

FIG. 2. **a**: Graphical representations of the spin's time-dependent phase profile as it progresses through the acquisition process in one-dimensional spatially encoded imaging. Note that although the entire sample is excited, only spins located within the blue regions contribute to the signal at each instance in time. The reason for this is readily visible in (**b**), showing the effects of these phase profiles on unity magnetization vectors: only within blue regions does the phase vary slowly enough to allow the spins to add constructively. Also evidenced in this cartoon is the inherent oversampling of this acquisition method, as expressed by the overlapping of the blue regions between successive times. **c**: Time- and space-dependent profiles defining the $\hat{\mathbf{P}}(y,t)$ matrix involved in the SR reconstruction, given by the phase (left) and amplitude (right) profiles. $\hat{\mathbf{P}}(y,t)$ is readily calculated for any given set of experimental parameters (in the present set, plots arise from $L_y = 3.2$ cm, $T_{acq} = 100$ ms).

Super-Resolved Spatially Encoded 2D MRI: Numerical Implementation and Performance

Given the nature of the data grid that will eventually arise from the spatially encoded "hybrid" single-scan 2D sequence in Fig. 1e, it is convenient to recast the arguments just made into a discrete form. Keeping for simplicity the arguments confined to the y axis—as in the end this spatially encoded dimension will be the sole axis that will have to be addressed by the implementation of the SR algorithm—we denote by $M = L_y/\Delta y$ the initial number of pixels afforded by the simple magnitude calculation in Eq. 3 and by N, the overall number of sampled points along this axis. In most practical implementations of these MRI experiments, one would then have $N = 2N_{pe}$ (cf. Fig. 1e) and a signal oversampling defined by a factor $N/M > 1$. In order to exploit this oversampling using SR, we cast Eq. 2 into a discrete matrix form:

$$\vec{S}(t_i) = \sum_{k=1}^{M_{SR}} \hat{\mathbf{P}}(y_k, t_i)\vec{\rho}_{SR}(y_k), \quad i = 1, \ldots, N. \quad [5]$$

Here $\vec{S}(t_i)$ is the experimentally measured signal vector composed of N complex sampled points,

$\{\vec{\rho}_{SR}(y_k)\}_{k=1\ldots M_{SR}}$ is a column vector of $M_{SR} > M$ real numbers making up the SR enhanced image and whose values we are trying to reconstruct, and $\hat{\mathbf{P}}(y_k, t_i)$ is a complex matrix depending on the phase terms ϕ_{exc} (y) and ϕ_{acq} (y,t) given by Eqs. 1 and 2. This matrix contains all the dynamic spin evolution information accumulated throughout the MRI experiment and can be calculated a priori based on the sequence parameters. The challenge of enhancing the spatial resolution can thus be cast into solving the linear set of equations in Eq. 5 in order to obtain the "super-resolved" $\{\vec{\rho}_{SR}(y_k)\}$ vector. This enhancement will naturally be limited by the signal oversampling ratio, but since all practical cases incorporate ample oversampling, we find it often feasible to reach the $M_{SR} = N$ limit. This means that every data point sampled on $\vec{S}(t_i)$, can eventually contribute to define a spatial element in the $\{\vec{\rho}_{SR}(y_k)\}_{k=1\ldots N}$ image.

Solving in this manner for a $\vec{\rho}_{SR}$ vector is in fact a least-square fitting process; an operation that, while simple in principle, is known to be numerically unstable within the context of MR. Several regularization approaches have been proposed for inverting MR time-domain problems like this in realistic cases (25–28), each one presenting its own opportunities and challenges, depending on the available signal-to-noise ratio. In the present case, however, we found this least-square fitting to be unusually stable, even without invoking any regularization methods. We ascribe this behavior to the fact that the quadratic phase profile arising from the spatial encoding endows the $\hat{\mathbf{P}}(y_k, t_i)$ matrix with a low condition number, preventing the onset of numerical instabilities. This feature is rationalized in Fig. 2c, which depicts the $\hat{\mathbf{P}}$ matrix phase and amplitude components, arising upon binning the originally continuous (y,t) space into the discrete grid supporting Eq. 5. Notice that the rapid phase variations in all but the stationary points of the $e^{i[\phi_{exc}(y)+\phi_{acq}(y,t)]}$ phasors concentrate the contributing amplitudes along a narrow band by the matrix's diagonal; this, in turn, precludes the onset of potential instabilities arising from distant $\vec{\rho}(y)$ contributions, located far from the stationary y-point. As for the specific fitting approach employed to solve Eq. 5, we chose a least-square error minimization of the unknown target function $\vec{\rho}_{SR}(y)$ based on the conjugate gradient formalism, implemented by the Inverse NFFT CGNR iterative algorithm (29).

MATERIALS AND METHODS

To evaluate the algorithms described in this work, the results of SR-enhanced spatially encoded 2D single-scan images were compared against those arising from a blipped EPI sequence. These experiments were based on the sequences introduced in Fig. 1e,f, they focused on phantom samples ($CuSO_4$-doped H_2O; acetone/chloroform in a 1:5 ratio) and on mice, and they were executed at 7 T on a 300/89 Varian VNMRS vertical imaging system (Varian Associates, Inc., Palo Alto, CA) using a quadrature-coil probe having a field of view of $30 \times 30 \times 46\text{mm}^3$. Mice were maintained and handled under protocols approved by the Weizmann Institute's Animal Care and Use Committee. All radiofrequency pulses used in the various sequences were designed using the Shinnar-LeRoux algorithm (30). Calculations and postexperimental data processing were implemented using custom-written MatLab (The MathWorks Inc., Natick, MA) software packages. (All the imaging sequences and postprocessing codes used in this study are available upon request.)

All the considerations made above focused on reconstructing $\vec{\rho}_{SR}(y)$ along one single spatial dimension; many different sequences can actually be devised to exploit these one-dimensional SR arguments within the context of multidimensional imaging. In the present study, we relied on a straightforward "hybrid" 2D implementation of the single-scan acquisition (13,15,16), whereby spatial encoding and conventional k-encoding act along orthogonal y and x axes, respectively (Fig. 1e). Slice selection was achieved by this sequence by the insertion of a narrow-banded 180° refocusing pulse along the third axis; further details about the actual sequence parameters employed in each experiment are given in the corresponding figure captions. The general performance characteristics of these hybrid pulse sequences have been discussed in the literature and hence will not be summarized in their entirety here. The sole aspect worth remarking on again is the immunity that this approach exhibits against field and shift heterogeneity distributions, vis-à-vis the effects that EPI exhibits along its low bandwidth dimension (14,15). It is the combination of this robustness and of SR's image-enhancing capabilities that accounts for the substantial quality gaps between the spatially encoded and the EPI single-scan images shown in Fig. 1b and c, as well as in the experimental examples given below.

In terms of processing the actual experimental data sets, the SR reconstruction proceeded as described in the Theory section, apart from a need to suitably prealign data originating from positive and negative echoes prior to its implementation. This requirement was absent when the spatially encoded processing was based on a straightforward magnitude $|S(t)|$ calculation, yet is needed if one wishes to "pool" together the oversampled data acquired under the action of both the $+G_{ro}$ and $-G_{ro}$ readout gradients. This alignment procedure is analogous to the one we used upon processing the blipped EPI signals for handling (that is, decreasing or altogether eliminating) the half-Nyquist ghost patterns associated to this technique. The SR processing was performed using a standard desktop personal computer and demanded a total computation time of less than a second for processing any of the 2D data sets hereby displayed. Repeated runs on several 2D test cases revealed that the number of least-square iterations required to converge onto a high-resolution profile was on the order of one to four, reflecting the robustness of the SR algorithm. This convergence could be achieved equally fast starting with a magnitude representation of the $|S(t)|$ data as initial guess of $\rho_{SR}(y)$ or, alternatively, starting from an all-zero image vector.

RESULTS AND DISCUSSIONS

Figures 3–5 complement the summary shown in Fig. 1a-d regarding the advantages arising from the use of SR

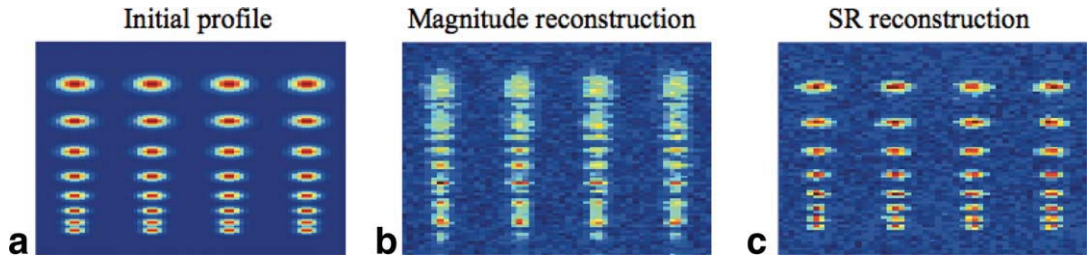

FIG. 3. Ability of the SR algorithm to restore high-definition 2D MR images in the presence of noise. **a**: Initial synthetic profile containing the target features to be resolved. **b**: Image arising from simulating the effects of the sequence illustrated in Fig. 1e on phantom (**a**), to which random noise was added to bring the effective signal-to-noise ratio to ca. 5. Data processing consisted of a one-dimensional FT along the RO axis and a |S(t)| modulus calculation of the resulting signal. **c**: 2D profile arising upon applying the SR algorithm to the data in (**b**). [Color figure can be viewed in the online issue, which is available at www.interscience.wiley.com.]

algorithms, by focusing on three additional aspects of this new approach to single-scan 2D MRI. Figure 3 demonstrates the ability of this sequence and algorithm to reconstruct finely detailed images even when these possess poor sensitivity. We chose to exemplify this robustness based on spin simulations expected to arise from the sequence in Fig. 1e for a numerically synthesized phantom (Fig. 3a). To an ideal NMR signal calculated for this phantom, noise was added until arriving to a signal-to-noise ratio ≤ 5. Whereas images reconstructed on the resulting data by the normal magnitude-mode calculation possess a poor definition (Fig. 3b), the SR algorithm easily restores the fineness and details of the original pattern (Fig. 3c). Notice as well the algorithm's robustness, which enhances equally well features characterized by different sensitivities. These are all reflections, once again, of the well-conditioned nature of this numerical reconstruction problem

Figure 4 highlights a different aspect of the method, concerning its robustness vis-à-vis field inhomogeneities (ΔB_o). Its panels involve a series of experiments performed on a cross-shaped phantom subject to frequency dispersions arising from different ΔB_o distributions, generated by better/worse shimming conditions and characterized by phase maps run in conjunction with each experiment (not shown). These results demonstrate the substantially higher image quality afforded by the new SR-based processing approach (Fig. 4b,f) both when compared against magnitude-processed spatially encoded data (Fig. 4a,e) and against EPI counterparts (Figs. 4c,g). Notice that the SR-based reconstruction process can deliver these improved images without changing the acquisition parameters of the original spatially encoded sequence, or without any information about the nature of the $\Delta B_o(x,y)$ field-map distribution. All that SR does is impart its image-improvement processing characteristics

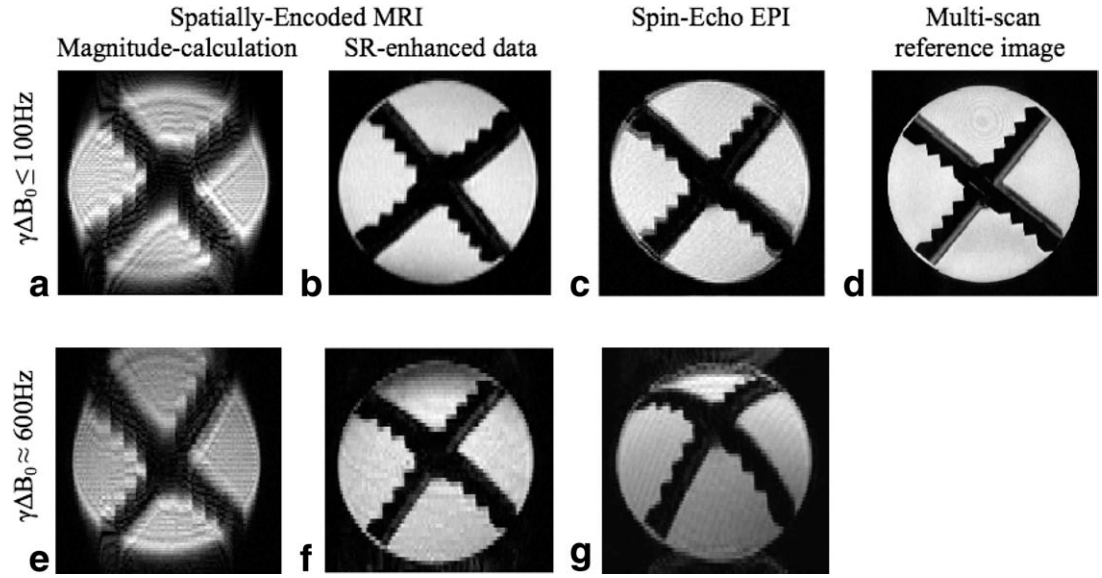

FIG. 4. Single-scan 2D images of a $CuSO_4$-doped, water-filled, cross-shaped phantom ($25 \times 25 mm^2$). **a,e**: Conventionally processed (FT along *x*, magnitude along *y*) spatially encoded MRI images collected under homogeneous and inhomogeneous amplitude of static field conditions (sequence in Fig. 1e with 0.5mm slice selection along z; $T_{exc} = 3$ ms; $R = 32$ kHz/ms; $T_{se} = 4$ ms; $T_{acq} = 100$ ms (top)/50 ms (bottom); $\Delta x = 0.25$mm; $\Delta y = 1.9$mm). **b,f**: SR-based reconstruction of the data, taking the voxel size Δy from 1.9mm to 0.35mm (top)/0.5mm (bottom). **c,g**: Spin-echo EPI image collected under similar conditions (sequence in Fig. 1f with 0.5mm slice; $T_{exc} = 2$ ms; $T_{se} = 4$ ms; $T_{acq} = 100$ ms (top)/50 ms (bottom); $\Delta x = 0.25$mm; $\Delta y = 0.5$mm). **d**: A reference multiscan gradient-echo image (acquisition time = 30 sec).

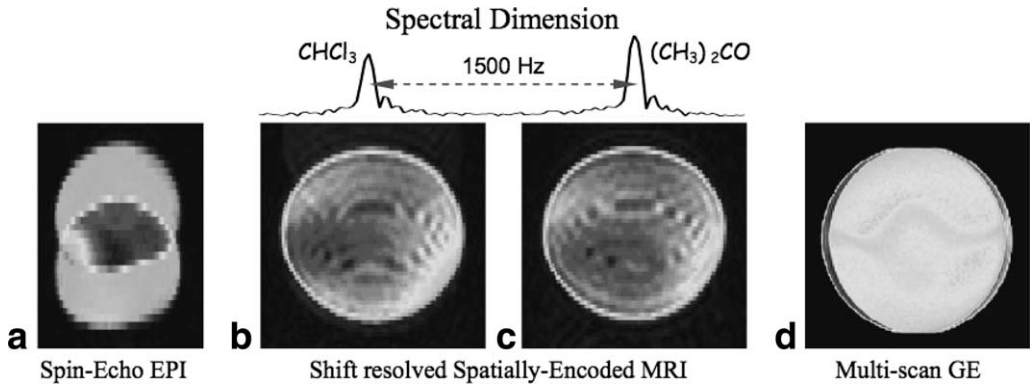

FIG. 5. Single-scan 2D images of a mixed chloroform-acetone phantom tube (25 × 25mm^2), evaluating the relative performance of spatially encoded versus EPI method when dealing with two chemical sites. **a**: EPI image (field of view 25 × 45mm^2) acquired using the sequence in Fig. 1f, showing the typical shift distortions arising along the phase-encoded dimension from multiple chemical sites (sequence in Fig. 1f with 1mm slice; $T_{exc} = 2$ ms; $T_{se} = 4$ ms; $T_{acq} = 24$ ms; $\Delta x = 0.4$mm; $\Delta y = 1.2$mm). **b,c**: SR-enhanced 2D images arising from the chloroform (**c**) and acetone (**d**) peaks, upon digital filtration of the spectral dimension (top) (sequence in Fig. 1e with 2mm slice; $T_{exc} = 3$ ms; $R = 48$ kHz/ms; $T_{se} = 4$ ms; $T_{acq} = 23$ ms; $\Delta x = 0.33$mm; $\Delta y = 1$mm). Both SR-enhanced images and the corresponding spectrum on top originate from the same single-scan data (14). **d**: Reference multiscan gradient-echo image, still evidencing minor shift artifacts along its RO axis (acquisition time = 40 sec).

to the built-in immunity of a sequence relying on stronger blipped gradients than its conventional EPI counterpart (15).

Figure 5 presents a final set of comparisons, this time involving 2D images collected on a phantom containing two distinct chemical sites. This sample was constructed by mixing two liquids coexisting in the same volume, albeit resonating at different frequency offsets. This model mimics the case of tissues placed at high fields with coexisting water- and fat-derived signals and gave typical distortions in the spin-echo EPI image (Fig. 5a). By contrast, using the phase information stored along the spatially encoded axis, the hybrid MRI sequence of Fig. 1e can easily distinguish among the chemical sites that contribute to the total signal. Extracting this information does not require any a priori information; instead, as discussed in Tal and Frydman (14), this additional spectral dimension emerges from the fact that, unlike EPI, the hybrid sequence does not rely on an FT for extracting its imaging information along the spatially encoded dimension. This provides an additional degree of freedom: phase information that by FT can yield the chemical shift distribution arising from the sample. This NMR spectrum will be characterized for each x-coordinate by Nyquist parameters associated to the $2N_{pe}$-point vector digitized over a time T_{acq} for the spatially encoded y-dimension. Filtration at a particular chemical shift frequency band, inverse FT, and application of the SR-enhancing protocol on the resulting single-site hybrid set can then originate separate 2D images for each of the resolved chemical sites in the sample at no extra cost in the experiment's complexity (Fig. 5b and c). It is important to note that, given the fact that the chemical-shift filtration and the SR procedures employed to produce these images are to a large extent independent of one another, the use of both techniques on the same data set does not detract SR's imaging enhancing qualities. Furthermore, it has been discussed elsewhere how different field-inhomogeneity compensating algorithms could be included by modifications on the basic imaging sequence shown in Fig. 1e (14–16); all these procedures can also be exploited if and when the frequency separation between the shifted NMR peaks becomes spatially heterogeneous.

CONCLUSIONS

The examples in this paper illustrate some of the advantages that may result from incorporating SR-based protocols into the processing of data arising from single-scan 2D spatially encoded MRI. While similar to EPI in their pulse-sequencing format and hardware requirements, the different spin physics on which these acquisition approaches rely yield a resolving power that equals or exceeds that afforded by the FT-based methods while offering a higher robustness vis-à-vis field inhomogeneities, susceptibility distortions, and chemical shifts artifacts. When combined with the capabilities of SR processing algorithms, all of these spatial encoding advantages can be exploited to endow images with a superior, EPI-like spatial resolution. Implementing the SR algorithms as described in this work does not entail the need of any a priori input about the presence or nature of potential nonidealities. On the other hand, we are currently exploring whether the incorporation of these and/or of additional parameters into this algorithm could be exploited in order to improve the quality or sensitivity of the resulting SR-enhanced images. One could, for example, exploit a priori knowledge about T_2* effects, chemical shifts, Δ amplitude of static field or Δ amplitude of radiofrequency field inhomogeneity distribution maps, multiple receiving coils sensitivity maps, or the anatomy of the object in question and incorporate all this information onto the transformation matrix $\hat{\mathbf{P}}$ to correct for their corresponding features or artifacts. We hope to report further on these and other properties of this new processing approach in future studies.

From a practical standpoint, two main consequences are important to remark on in connection with reliance on SR-enhancing protocols for retrieving spatially encoded images, particularly as opposed to the use of simple magnitude-calculation protocols. One concerns the higher spatial resolution that this algorithm can make available, entailing an improvement defined by the oversampling ratio *N/M*. As detailed in the introduction, resolution in spatially encoded experiments is usually given by the excitation characteristics (G_{exc}, T_{exc}), rather than by acquisition ones as in FT-based methods. The fact that the excitation happens in these experiments while spins are subject to a 90° chirped encoding pulse means that the SR-derived image enhancement can be traded for a reduction in either the duration and/or bandwidth demanded from these initial pulses; i.e., in exchange for a reduction in the experiment's SAR by a factor of *N/M*. The consequences derived from these gains upon exploiting these methods for human functional MRI studies will be described elsewhere. A second consequence worth remarking on concerns the better signal-to-noise ratio that SR-processed images display when compared with their simple magnitude-calculation counterparts. While a full analysis of this improvement is still in progress, it is apparent that this also depends on the oversampling ratio as approximately $\sqrt{N/M}$, thus making up for the signal-to-noise ratio losses that, under equal G_{acq} conditions, spatially encoded methods may have vis-à-vis Fourier-based counterparts (12–14).

ACKNOWLEDGMENTS

The authors thank Yoav Shrot for pointing out Kunis (29), and for other helpful discussions. This research work was supported by the Israel Science Foundation (ISF 447/09), by a Helen Kimmel Award for Innovative Investigation, and by the generosity of the Perlman Family Foundation.

REFERENCES

1. Beutel J, Kundel L, Van Metter L. Handbook of medical imaging. Bellingham, WA: SPIE Press; 2000. pp 373–464.
2. Mcrobbie DW, Moore EA, Graves MJ, Prince MR. MRI: from picture to proton. New York: Cambridge University Press; 2007.
3. Ogawa S, Tank DW, Menon R, Ellerman JM, Kim SG, Merkle H, Ugurbil K. Intrinsic signal changes accompanying sensory stimulation: functional brain mapping with magnetic resonance imaging. Proc Natl Acad Sci U S A 1992;89:5951–5955.
4. Ogawa S, Lee TM, Kay AR, Tank DW. Brain magnetic resonance imaging with contrast dependent on blood oxygenation. Proc Natl Acad Sci U S A 1990;87:9868–9872.
5. Charms RC. Applications of real-time fMRI. Nat Rev 2008;9:720–729.
6. Basser PJ, Jones DK. Diffusion-tensor MRI: theory, experimental design and data analysis: a technical review. NMR Biomed 2002;15: 456–467.
7. Mansfield P. Multi-planar image formation using NMR spin echoes. J Phys C 1977;10:L55–L58.
8. Schmitt F, Stehling MK, Turner R. Echo-planar imaging: theory, technique and applications. Heidelberg: Springer-Verlag; 1998.
9. Bernstein MA, King KF, Zhou XJ. Handbook of MRI pulse sequences. Elsevier Academic Press; 2004.
10. Frydman L, Scherf T, Lupulescu A. The acquisition of multidimensional NMR spectra within a single scan. Proc Natl Acad Sci U S A 2002;99:15858–15862.
11. Mishkovsky M, Frydman L. Principles and progress in ultrafast multidimensional nuclear magnetic resonance. Annu Rev Phys Chem 2009;60:429–448.
12. Shrot Y, Frydman L. Spatially encoded NMR and the acquisition of 2D magnetic resonance images within a single scan. J Magn Reson 2005;172:179–190.
13. Tal A, Frydman L. Spatial encoding and the acquisition of high definition MR images in inhomogeneous magnetic fields. J Magn Reson 2006;181:179–194.
14. Tal A, Frydman L. Spectroscopic imaging from spatially-encoded single-scan multidimensional MRI data. J Magn Reson 2007;189: 46–58.
15. Ben-Eliezer N, Shrot Y, Frydman L. High-definition single-scan 2D MRI in inhomogeneous fields using spatial encoding methods. Magn Reson Imaging 2010;28:77–86.
16. Chamberlain R, Park JY, Corum C, Yacoub E, Ugurbil K, Jack CR Jr, Garwood M. RASER: a new ultrafast magnetic resonance imaging method. Magn Reson Med 2007;58:794–799.
17. Kunz D. Use of frequency-modulated radiofrequency pulses in MR imaging experiments. Magn Reson Med 1986;3:377–384.
18. Pipe JG. Spatial encoding and reconstruction in MRI with quadratic phase profiles. Magn Reson Med 1995;33:24–33.
19. Pipe JG. Analysis of localized quadratic encoding and reconstruction. Magn Reson Med 1996;36:137–146.
20. Irani M, Peleg S. Improving resolution by image registration. Graphical Models Image Processing 1990;53:231–239.
21. Irani M, Peleg S. Motion analysis for image enhancement: resolution, occlusion, and transparency. Vis Com Image Repr 1993;4:324–335.
22. Hell SW. Microscopy and its focal switch. Nat Methods 2009;6: 24–32.
23. Shechtman E, Caspi Y, Irani M. Space-time super-resolution. IEEE Trans Pattern Anal Machine Intell 2005;27:531–545.
24. Guillermin V, Sternberg S. Geometric asymptotics. American Mathematical Society; 1990.
25. Sibisi S, Skilling J, Brereton RG, Laue ED, Staunton J. Maximum entropy signal processing in practical NMR spectroscopy. Nature 1984; 311:446–447.
26. Manassen Y, Navon G. Nonuniform sampling in NMR experiments. J Magn Reson 1988;79:291–298.
27. Hoch J C, Stern A. NMR data processing. New York: Wiley-Liss; 1996.
28. Mandelshtam VA. FDM: the filter diagonalization method for data processing in NMR experiments. Prog Nucl Magn Reson Spectrosc 2001;38:159–196.
29. Kunis S. Nonequispaced FFT generalisation and inversion. PhD thesis. Lubeck, Germany: University of Lubeck; 2006.
30. Pauly JM, LeRoux P, Nishimura DG, Macovski A. Parameter relations for the Shinnar–LeRoux selective excitation pulse design algorithm. IEEE Trans Med Imaging 1991;10:53–65.